Computers in Biology and Medicine 155 (2023) 106655

Contents lists available at ScienceDirect

Computers in Biology and Medicine

journal homepage: www.elsevier.com/locate/compbiomed

Manifold analysis of the P-wave changes induced by pulmonary vein isolation during cryoballoon procedure

Laura Martinez-Mateu [a,*], Francisco M. Melgarejo-Meseguer [a], Sergio Muñoz-Romero [a,b], Francisco-Javier Gimeno-Blanes [c,b], Arcadi García-Alberola [d], Sara Rocher-Ventura [e], Javier Saiz [e], José Luis Rojo-Álvarez [a,b]

[a] Departamento de Teoría de la Señal y Comunicaciones y Sistemas Telemáticos y Computación, Universidad Rey Juan Carlos, Madrid, Spain
[b] D!lemmaLab Ltd Startup, Fuenlabrada, Spain
[c] Departamento de Ingeniería de Comunicaciones, Universidad Miguel Hernández, Elche, Spain
[d] Unidad de Arritmias, Hospital Clínico Universitario Virgen de la Arrixaca - IMIB, Murcia, Spain
[e] Centro de Investigación e Innovación en Bioingeniería, Universitat Politècnica de València, Valencia, Spain

ARTICLE INFO

Keywords:
Ablation
Atrial fibrillation
P-wave
Manifold analysis
Signal processing
Simulation

ABSTRACT

Background/Aim: In atrial fibrillation (AF) ablation procedures, it is desirable to know whether a proper disconnection of the pulmonary veins (PVs) was achieved. We hypothesize that information about their isolation could be provided by analyzing changes in P-wave after ablation. Thus, we present a method to detect PV disconnection using P-wave signal analysis.

Methods: Conventional P-wave feature extraction was compared to an automatic feature extraction procedure based on creating low-dimensional latent spaces for cardiac signals with the Uniform Manifold Approximation and Projection (UMAP) method. A database of patients (19 controls and 16 AF individuals who underwent a PV ablation procedure) was collected. Standard 12-lead ECG was recorded, and P-waves were segmented and averaged to extract conventional features (duration, amplitude, and area) and their manifold representations provided by UMAP on a 3-dimensional latent space. A virtual patient was used to validate these results further and study the spatial distribution of the extracted characteristics over the whole torso surface.

Results: Both methods showed differences between P-wave before and after ablation. Conventional methods were more prone to noise, P-wave delineation errors, and inter-patient variability. P-wave differences were observed in the standard leads recordings. However, higher differences appeared in the torso region over the precordial leads. Recordings near the left scapula also yielded noticeable differences.

Conclusions: P-wave analysis based on UMAP parameters detects PV disconnection after ablation in AF patients and is more robust than heuristic parameterization. Moreover, additional leads different from the standard 12-lead ECG should be used to detect PV isolation and possible future reconnections better.

1. Introduction

Atrial Fibrillation (AF) refers to a supraventricular tachyarrhythmia characterized by uncoordinated atrial electrical activation of the atria with a lack of mechanical contraction [1]. The electrocardiogram (ECG) represents the electrical activity of the heart, and it is comprised of a P-wave, a QRS complex, and a T-wave produced by atrial depolarization, ventricular depolarization, and ventricular repolarization, respectively [2]. The ECG during AF typically shows an irregular ventricular rhythm, absence of discrete P-waves, and irregular and swift atrial activity. The underlying mechanisms of this arrhythmia are not completely understood. However, the rapid firing of electrical foci located in myocardial sleeves entering the pulmonary veins (PVs) seems to play an essential role in the genesis and maintenance of AF, as well as other complex electrical, histologic, and anatomic changes of the atria. It is currently assumed that the primary goal of the AF ablation procedure is to achieve complete and long-lasting electrical isolation of all PVs. This disconnection is obtained by performing a transmural lesion (full-thickness lesion that completely disconnects PV [3]) in the portion of the left atrium (LA) surrounding the ostium of each PV using radiofrequency or cryothermal energy. The application techniques of this second case have evolved throughout history, and the Cryoballoon procedure is currently usual and widely described in the

* Corresponding author.
E-mail address: laura.martinez.mateu@urjc.es (L. Martinez-Mateu).

https://doi.org/10.1016/j.compbiomed.2023.106655
Received 27 September 2022; Received in revised form 17 January 2023; Accepted 8 February 2023
Available online 10 February 2023

literature due to its advantages over other methods, especially for the isolation of the PVs [4]. The electrical activity in the PVs is evaluated during the ablation procedure using a circular multielectrode catheter inserted into the vein. The ablation is successful when all PVs are electrically isolated from the LA tissue. However, recurrences of the AF after an acutely effective ablation procedure are not uncommon, and the clinician must know if the recurrence may be related to an electrical reconnection of one or more PVs or a different mechanism. A new invasive procedure is required to obtain this information, placing a diagnostic catheter again in each PV and checking their electrical connection with the surrounding LA.

A non-invasive technique giving information on the electrical status of the PVs would be highly desirable to avoid the need for this transvenous invasive approach. The ablation procedure abolishes the electrical activity of the PVs and surrounding LA areas, thus modifying the characteristics of the P-wave in the ECG. Changes in the P-wave duration, dispersion, and morphology have been described after a successful ablation, reflecting the loss of electrical activity in the PV area [5,6]. More precise detection and definition of these changes might be helpful to recognize, using a non-invasive technique, if the PVs are still electrically isolated in patients with arrhythmia recurrences after a previous acutely successful AF ablation procedure.

Therefore, the main goal of this study is the non-invasive detection of PV disconnection after a cryoballoon procedure. For this purpose, we compare conventional feature extraction and manifold analysis of the P-waves. In addition, we use a virtual patient to explore if, apart from the standard leads, other signals over the torso surface might help to detect P-wave changes after the ablation procedure and, thus, PV disconnection.

The outline of the document is as follows. Next section summarizes related works. Later, a general notation, ECG datasets (control and AF ablation groups), and advanced simulations are described. Then, preprocessing stages of the ECG are summarized, the ECG-based P-wave biomarkers are defined, and the UMAP algorithm and its characteristics are detailed. Section 4 shows the results corresponding to ECG preprocessing and quality control, ECG datasets, and in-silico predictions. Results of the heuristic biomarkers are then compared with the results of the UMAP-based biomarkers in Section 5. Finally, results are discussed, and conclusions are drawn.

2. Related works

ECG analysis in general, and of the P-wave in particular, requires a pre-processing stage followed by the heartbeat segmentation before features extraction [7]. Therefore, wave delineation algorithms are commonly used for heartbeat segmentation to obtain morphological differences and parameters identified in the clinical literature as characteristic of different pathologies. In this direction, relevant articles are published annually that present improvements and new delineation algorithms [8,9], which use different heuristic characteristics and delineation strategies to examine both the variables and their changes in different circumstances. Occasionally, this delineation can exhibit noisy behavior, significant sensitivity to thresholds and design parameters, and variability between patients. For this reason, in this work, it is proposed to use the characteristics obtained from multiple learning techniques to extract the relevant information from P-waves automatically. To do this, we evaluate the potential of the recently proposed method of Uniform Manifold Approximation and Projection (UMAP) [10,11], which is capable of compressing a high-dimensional input space into a low-dimensional latent space, where the most relevant and intrinsic characteristics of a plurality of signals are consolidated.

The standard 12-lead ECG usually includes all the information needed for diagnosis. However, in some cases, cardiac phenomena can be unnoticed when using the standard 12-lead ECG. The body surface potential mapping (BSPM) can overcome this limitation thanks to the increased number of electrodes used. While the standard 12-lead ECG records the cardiac electrical activity from 9 sites, the BSPM records it on the entire torso surface, providing further regional information and even showing where in the heart an event might be located [12]. For this reason, we surmised in this work that BSPM might be useful to see changes in P-waves after an ablation procedure and provide additional information to the standard 12-lead ECG. We use a virtual patient to analyze the best region of the torso to observe those changes.

Cardiac computational models were developed to improve the understanding of cardiac electrophysiology and arrhythmias. Nowadays, the heart electrical activity can be multiscale modeled from the cellular level to the body surface. Therefore, computational models simulate the flux of currents through the ionic channels in the cellular membrane, the resultant membrane potential, its spreading throughout the myocardium, and, finally, the propagation of the electrical signals generated by the heart and their registration at the torso surface [13]. So, using computational models, we can build virtual patients. In the last years, the use of atrial models in AF-related studies has exponentially increased [14], demonstrating that they can be useful and powerful tools that complement research based on clinical recordings.

3. ECG datasets and simulations

In order to detect P-wave changes in AF ablation patients, we studied the P-waves characteristics and their possible variations in duration and morphology before and after a cryoablation procedure. An example of the P-waves stability for healthy individuals and of P-waves changes after an ablation procedure is shown in Fig. 1(a–b). A two-fold approach was followed to comprehensively analyze the scope of conventional and UMAP-based feature extraction methods. On the one hand, a clinical dataset was assembled to provide the natural conditions of P-wave recordings in clinical environments. On the other hand, detailed computational simulations were conducted to provide a noise-free environment and extend the analysis of the 12-lead ECG recordings to the complete torso. We start by establishing a standard notation for all the subsequent sections.

3.1. Notation

Let S denote a two-dimensional continuous surface (or manifold) in a three-dimensional space, and let $\mathbf{r}_S$ be the set of points in this surface, which is defined as

$$\mathbf{r}_S \equiv \{\mathbf{r} \in S, \quad S \in \mathbb{R}^3\} \tag{1}$$

where $\mathbf{r}$ stands for the position vector of any point in the three-dimensional space. In our case, surface S can, for instance, represent the torso T or the epicardium E, and the potential fields changing with time on them are denoted as $v_T = v(\mathbf{r}_T, t)$ and $v_E = v(\mathbf{r}_E, t)$.

A geometrical mesh can represent a continuous surface due to discretizing it. For instance, by using a set of sensors on S, a single measurement point i on a mesh surface can be denoted as

$$\mathbf{s}_n(\mathbf{r}) = \mathbf{r}_S \cdot \delta(\mathbf{r} - \mathbf{r}_n) \tag{2}$$

where $\delta(\mathbf{r})$ is a Dirac's delta function in the spatial domain, and $\{\mathbf{s}_n, n = 1, \ldots, N_S\}$ is a discrete set of N_S points where measures are sampled on surface S, and they are the nodes of this mesh. The measurement mesh on S is given by

$$\mathbf{r}_S^m(\mathbf{r}) = \sum_{n=1}^{N_S} \delta(\mathbf{r} - \mathbf{r}_n) \tag{3}$$

where superindex m refers to the mesh operator given by the discrete set of measurement points.

With this notation, the epicardium (the torso) surface operator is given by $\mathbf{e}_n(\mathbf{r})$ (by $\mathbf{t}_n(\mathbf{r})$) and its sampling mesh is given by $\mathbf{r}_E^m(\mathbf{r})$ (by

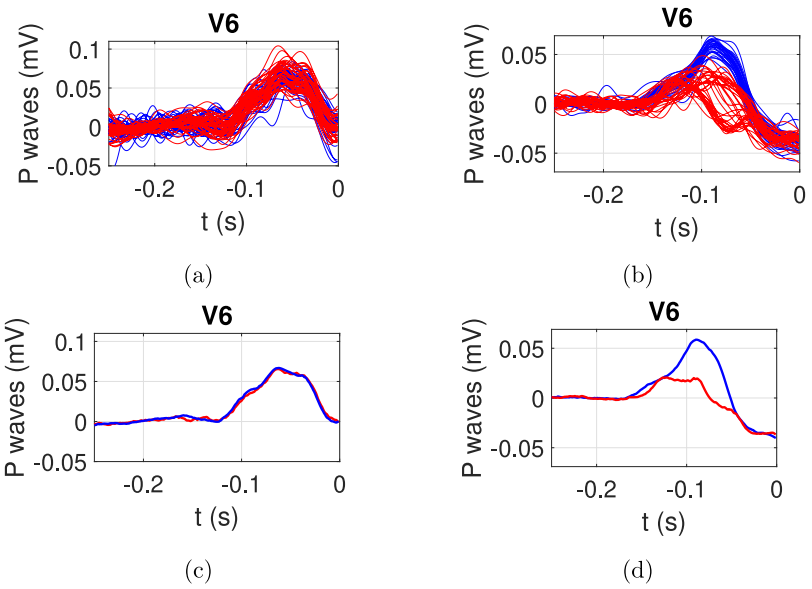

Fig. 1. P-waves corresponding to 30-s segments and their corresponding template. P-waves from a healthy (a) and AF ablation individual (b), and template corresponding to the P-waves from a healthy (c) and AF ablation (d) individual. P-waves/template corresponding to the first recording/pre-ablation recording in blue; P-waves/template corresponding to the second recording/post-ablation recording in red.

$\mathbf{r}_T^m(\mathbf{r})$). Accordingly, a set of points sampled on the torso mesh is just given by

$$v_T^m = v_T\ \mathbf{r}_T^m(\mathbf{r}) \tag{4}$$

and it consists of a set of spatial samples $\{v_{T,n}; n = 1, \ldots, N_T\}$. These detailed torso sampling can be obtained either with advanced BSPM or with detailed simulations including the torso.

If we think of $\mathbf{l}_j$ as a different set of partially virtual points, with $j = 1, \ldots, 12$, which are associated with the measurement of the standard 12-lead ECG, we have that

$$v_T^l = v_T\ \mathbf{l}_j^m(\mathbf{r}) \tag{5}$$

gives us a representation of the potentials measured in the conventional ECG, denoted as v_T^l.

3.2. ECG datasets

In this work, a patient database compounded by 35 electrocardiographic records was collected and analyzed by expert clinicians from Hospital Clínico Universitario Virgen de la Arrixaca (HCUVA) in Murcia (Spain). These records were selected, based on the inclusion criteria, from a more extensive database compounded from studies performed in HCUVA Electrophysiology Laboratory in the last years. The database was divided into two groups, with the following inclusion criteria: the control group (19), where no ablation or drug test was performed, and the AF ablation group (16), where PVs cryoablation with a cryoballoon was carried out. Two 30-second segments corresponding to the standard 12-lead ECG were extracted from each recording, with a time difference of about two hours. In the AF ablation group, the first segment corresponds to the procedure start (before any actuation was done), and the second corresponds to the procedure end (after PVs isolation). The device used to monitor the heart activity worked at 1 kHz sampling rate with a resolution of 5 μV.

3.3. Ablation simulations

A virtual patient was used to analyze changes between pre- and post-ablation recordings in synthetic P-waves generated through in-silico modeling (Fig. 2).

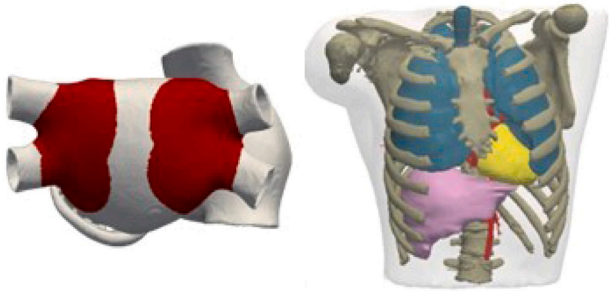

Fig. 2. Virtual patient. Left: 3D atrial model and cryoablation lesions (in red) after pulmonary veins isolation. Right: The torso model comprised seven regions, namely, the general torso, bones, blood, ventricles, atria, lungs, and liver.

Atrial electrical activity under paroxysmal AF (PAF) conditions was simulated in the realistic 3D model of the human atria, comprised of the main anatomical structures, atrial heterogeneity, and fiber direction [15]. The membrane electrical activity of every single atrial myocyte was modeled by the Courtemanche–Ramirez–Nattel ionic model [16], modified to incorporate the electrical remodeling observed under PAF conditions [17]. The monodomain formalism solved electrical activity in the 3D model with ELVIRA software and a constant time step of 0.01 ms [18]. After 1 min of stabilization of single-cell models at a basic cycle length of 500 ms, we stabilized the 3D atrial model for 10 s (20 pulses). Atrial activation was initiated by applying a stimulus of 28 pA/pF amplitude and 2 ms duration in the sinoatrial node region. Cryoablation lesions in the PVs were modeled by non-conductive tissue (see Fig. 2).

Once the atrial activity was simulated, extracellular potentials were computed over the whole torso model by approximating the bidomain formalism implemented in MATLAB (MathWorks, Natick, MA) with custom-made routines [15]. Bidomain equations can be partially decoupled by assuming equal anisotropy ratios for intracellular ($\mathbf{D}_i$) and extracellular ($\mathbf{D}_e$) conductance tensors

$$\mathbf{D}_e = \lambda \mathbf{D}_i \tag{6}$$

Therefore, in the heart domain, we can describe changes in the transmembrane potential (v_m) and the extracellular potential (v_e) [19] as

follows

$$\nabla(\mathbf{D}\nabla v_m) = C_m \frac{\partial v_m}{\partial t} + i_{ion} \tag{7}$$

$$\nabla(\mathbf{D}\nabla v_e) = -\frac{1}{1+\lambda}\nabla(\mathbf{D}\nabla v_m) \tag{8}$$

where $\mathbf{D} = \frac{1}{1+\lambda}\mathbf{D}_i$ is the equivalent conductivity tensor, i_{ion} is the transmembrane ionic current, and C_m is the membrane capacitance in the cellular model. In the two-steps bidomain approximation for the extracellular potential calculation, we first computed v_m in the heart tissue through Eq. (7) (monodomain formalism) and then approximated v_e through Eq. (8) in the whole torso volume. The following boundary conditions, which consider the heart to be immersed in a non-conducting bath, were applied,

$$\hat{\mathbf{n}} \cdot (\mathbf{D}\nabla v_m) = 0 \tag{9}$$

$$\hat{\mathbf{n}} \cdot (\mathbf{D}\nabla v_e) = 0 \tag{10}$$

Since the heart is immersed in the whole torso model, extracellular potentials were calculated in the entire domain (heart and torso outside the heart region). Therefore, we included the governing equations for the solid conductor associated with the torso and modified the boundary conditions at the heart-torso interface. Extracellular potentials in the torso domain were calculated by solving the following Laplace equation

$$\nabla(\mathbf{D}_T \nabla v_T) = 0 \tag{11}$$

where v_T and $\mathbf{D}_T$ are the extracellular potentials and the heterogeneous conductance tensor in the torso, respectively, and the boundary condition is $v_e = v_T$ (is $\hat{\mathbf{n}} \cdot (\mathbf{D}\nabla v_T) = 0$) at the heart-torso interface (at the torso-air non-flux interface). As a result, we obtained the P-waves by computing v_T at any virtual electrode located throughout the torso surface (v_T^m). Among these potentials, v_T^l corresponds to the signals at the standard 12-lead ECG. Simulated P-waves with a time resolution of 1 ms were registered during sinus rhythm propagation before cryoablation and after PVs isolation.

4. Processing and feature extraction

4.1. Signal conditioning and P-wave features

Potential Preprocessing. In a real environment, the measured potentials of interest are often embedded in noise from various other environmental electrical sources, which can be seen as noise with different properties. The potential field measured through the 12-lead ECG, $v_n^l(t)$, can be denoted as

$$v_n^l(t) = v_T^l(t) + H(t) + B(t) + R(t) \tag{12}$$

where H, B, and R represent the additive high-band pass Gaussian noise, the low-band pass baseline noise, and other noise contributions, respectively, for all the ECG leads. Different preprocessing stages are used to reduce noise in our measurements. We denote them here as signal operators $\boldsymbol{\Phi}_H$ and $\boldsymbol{\Phi}_B$, and they act on each ECG-measured signal separately so that

$$\hat{v}_T^l(t) = \boldsymbol{\Phi}_B(\boldsymbol{\Phi}_H(v_n^l(t))) \tag{13}$$

where $\hat{v}_T^l$ denotes the denoised potentials on the ECG channels. In our case, $\boldsymbol{\Phi}_H$ operator consisted of a low-pass filter (cut frequency 50 Hz, 7th-order Butterworth with zero phase), and $\boldsymbol{\Phi}_B$ was implemented with a spline-based trend removal with nodes spaced 0.75 s [20]. These kinds of noise are known to be the most present in ECG signals. For determining the parameters of ϕ_H operator, the filter order was scrutinized not to distort the signals, especially in the fast-changing waves (QRS complex), and the cut-off frequency was determined by ensuring that the morphology of P-waves and T-waves were respected and no aberrance was included. For determining the parameters of ϕ_B operator, the time-window separation between nodes corresponded to an interval generally including one heartbeat at most during sinus rhythm, and the residual baseline was represented to check that the QRS was not distorted [21]. A custom tool was created to represent these properties in all the cases. Several authors thoroughly checked the data quality in terms of this and other processing stages.

ECG Segmentation and P-wave Matrix. For the ECG leads, the segmentation process yields two matrices. On the one hand, operator $\boldsymbol{\Phi}_S$ denotes the segmentation from each measured cardiac signal to a matrix of beat templates, $\mathbf{X}_b^l$, in such a way that

$$\mathbf{X}_b^l = \boldsymbol{\Phi}_S(\hat{v}_T^l(t)) \tag{14}$$

denotes the matrix including in each row the averaged beat for each lead after QRS detection and beat alignment in the preprocessed 12-lead ECG for a given patient. This operator included a threshold criterion for compensating the positive or negative polarity of the QRS beat for each lead and patient. Once QRS complexes were temporally identified along the recording, the ECG was segmented into aligned beats, taking as a reference the position of the maximum value in the QRS complex, and averaged on a per-lead basis. Also, the confidence interval for every beat template was obtained on each signal.

The P-wave data matrix can be obtained from the beat data matrix using an additional operator $\boldsymbol{\Phi}_P$, as follows

$$\mathbf{P}^l = \boldsymbol{\Phi}_P(\mathbf{X}_b^l) \tag{15}$$

In the case of ECG recordings, the P-waves were aligned in the operator for yielding time support of 150 ms, ensuring to include of the P-wave but not the QRS onset. Also, a Hamming window was used for each P-wave to minimize the interference of ending T waves and QRS onset. The operator included P-wave median obtention, the confidence interval of which was also computed for each lead.

Note that we can obtain a P-wave data matrix from the torso measurements on the mesh in the simulations. We denote this P-wave matrix as $\mathbf{P}^T$, and in this case, no P-wave alignment is needed, and no Hamming window is used, as ventricular activity is not simulated. Signals can be restricted to the P-wave with a well-determined onset time.

P-wave Features. A set of features was engineered to extract the relevant information from P-wave templates. We can denote this feature extractor operator as $\boldsymbol{\Phi}_F$, and it represents the calculation of a new feature data matrix

$$\mathbf{F}^l = \boldsymbol{\Phi}_F(\mathbf{P}_{pre}^l, \mathbf{P}_{post}^l), \quad \mathbf{F}^T = \boldsymbol{\Phi}_F(\mathbf{P}_{pre}^T, \mathbf{P}_{post}^T) \tag{16}$$

where $\mathbf{F}^l$ ($\mathbf{F}^T$) denotes the feature data matrix for the 12-lead ECG (for the torso measurements on the torso mesh), obtained each in pre- and post-ablation conditions.

Each feature of the data matrix aims to measure some aspects of the nature of the P-wave. The following metrics were used:

1. f_1 was the correlation coefficient between the P-wave templates in pre- and post-ablation conditions.
2. f_2 was the mean absolute difference between the P-waves in pre- and post-ablation conditions.
3. f_3 was the correlation coefficient between the beat templates in pre- and post-ablation conditions.
4. f_4 was the difference in durations of the P-waves in pre- and pot-ablation conditions.
5. f_5 was the difference in amplitude of the P-waves peaks in pre- and post-ablation conditions.
6. f_6 was the difference in the area of the P-waves in pre- and post-ablation conditions.

Note that these features are obtained by a specific operator, which is integrated with the notation of $\boldsymbol{\Phi}_F$ operator. Hence, specific design decisions have to be made on the implementation of these operators.

On the other hand, the mean absolute error (MAE) among pre- and post-ablation P-waves was selected to account for the morphology

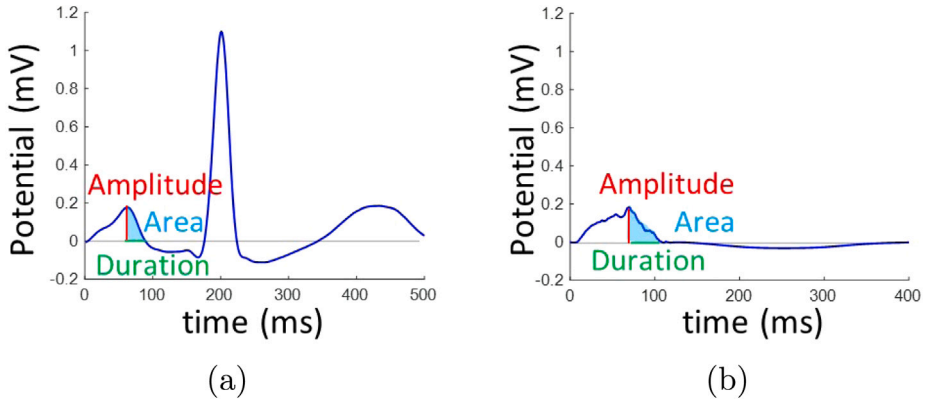

Fig. 3. Description of features f_4 (duration), f_5 (amplitude) and f_6 (area). (a) The whole beat template corresponds to a patient of the dataset. (b) Simulated P-wave.

changes which could be produced due to ablation. Moreover, its normalized value (NMAE) was computed for better individual comparison.

For comparing the pre- and post-ablation P-waves, a template comprised of the median P-wave of the complete recording was used (not applicable for simulated P-waves since only a beat was simulated). An example of the templates for the first and second recording of a control and an AF ablation individual is provided in Fig. 1(c–d). A Tukey window (0.75) was used to smooth the boundaries and reduce the border effect [22] due to T-waves or QRS-complexes, which might lie inside the P-wave window, with minimum impact on expected morphology. The circular correlation coefficient was obtained for each relative delay among both P-wave templates, and the delay yielding the maximum correlation coefficient was used to align them.

Regarding f_4 (duration), f_5 (amplitude), and f_6 (area) features, an adaptation of the Phasor Transform algorithm for delineation of ECG fiducial points was used [23]. Since PVs contribution corresponds to the last part of the P-wave [24], only the portion between the P-wave peak and the P-wave offset was considered for pre- and post-ablation comparison. The duration was defined as the difference between the time instants corresponding to the P-wave peak and P-wave offset; amplitude, as the P-wave peak; and area, as the integral of the P-wave limited to its duration (see Fig. 3). An unpaired t-test checked whether P-waves duration, amplitude, and area differed between the control and AF ablation groups. Also, a paired t-test checked whether the same variability could be observed among both registers within each group (95% confidence intervals).

In simulated signals, f_4, f_5, and f_6 were extracted from the P-wave at each point on the torso surface (v_T^m). In contrast, in clinical signals, these features were extracted from the P-wave template in each standard lead recording (v_T^l).

4.2. P-wave embeddings and UMAP-based features

The UMAP algorithm is a recently proposed manifold learning and dimension reduction technique. By using a theoretical framework based on Riemannian geometry and algebraic topology, this algorithm provides us with a non-linear mapping from the original input space to an embedded space where geometrical properties are preserved. The UMAP algorithm has been compared with other manifold learning techniques, such as t-distributed stochastic neighbor embedding (t-SNE) [25], which are often used for visualization purposes, and it is considered to better preserve the global structure of the original space after contraction to the embedding space, with good runtime performance. As UMAP has no computational restrictions on the embedding dimension, it is being used as a general dimension reduction technique for machine learning applications [26]. In summary, the UMAP algorithm performs dimension reduction by using the distances among the feature vectors of a dataset, denoted as $\mathbf{f}_n$, $\{n = 1, \ldots, N\}$. A strong assumption of the algorithm is that the feature vectors are uniformly distributed, which does not hold in many cases. However, it is partly compensated by tuning its free parameters in practice.

The algorithm can be summarized as follows [10]. As a first step, a *weighted directed graph* representation, denoted as $\mathbf{W}$ matrix, is built for the feature data, in which each feature vector is a vertex, and the distances among neighbors determine the edges. If we choose a K-order neighborhood, element $\mathbf{f}_n$ is linked to its K closest neighbors, $\mathbf{f}_n^1, \ldots, \mathbf{f}_n^K$, sorted out according to their distance to it. The neighborhood membership degree is established in terms of said distances, yielding the graph weights of the element to its K neighbors. The closest element $\mathbf{f}_n^1$ is assigned a membership of 1, and we denote its distance to $\mathbf{f}_n$ as λ_n. The weights are then defined by

$$w_n^k = \exp\left(-\frac{d(\mathbf{f}_n, \mathbf{f}_n^k) - \lambda}{\sigma}\right) \tag{17}$$

where σ is a free parameter of the algorithm. This expression represents a heat kernel, and its use was justified before [27]. The σ parameter ensures that for each data element $\mathbf{f}_n$, the density of the circle centered at $\mathbf{f}_n$ and with a radius equal to the distance to the K neighbors are about the same for each $\mathbf{f}_n$, which is accomplished by imposing

$$\sum_{k=1}^{K} w_n^k = \log_2(K) \tag{18}$$

After determining graph matrix $\mathbf{W}$, the *dimension reduction* into low-dimensional space $\mathbb{R}^d$ is done (typically, $d = 2$ or $d = 3$) by using the Laplacian eigenmaps. The nth feature vector is represented as a vector of coordinates $\mathbf{g}_n \in \mathbb{R}^d$. Their components are the coordinates concerning the eigenvectors of the Laplacian associated with $\mathbf{G}$, with the eigenvalues associated in descending order. Then, we can define a graph $\mathbf{W}'$ from $\mathbb{R}^d$ points, similarly to the previous step, except for the weights between $\mathbf{g}_n$ and $\mathbf{g}_m$, which are now defined by

$$w(\mathbf{g}_n, \mathbf{g}_m) = \frac{1}{1 + a\left(\|\mathbf{g}_n - \mathbf{g}_m\|^2\right)^b} \tag{19}$$

where free parameters a and b are chosen, so that function ψ realizes a smooth approximation of Ψ, being defined by

$$\psi(\mathbf{g}_n, \mathbf{g}_m) = \frac{1}{1 + a\left(\|\mathbf{g}_n - \mathbf{g}_m\|^2\right)^b} \tag{20}$$

$$\Psi(\mathbf{g}_n, \mathbf{g}_m) = exp\left(-\|\mathbf{g}_n - \mathbf{g}_m\|\right) \tag{21}$$

This smooth approximation allows us to *derive the cross-entropy* between $\mathbf{W}$ and $\mathbf{W}'$ graphs, which determines attractive and repulsive forces among the data, and a force-directed graph layout algorithm is subsequently computed. Then, each element of $\mathbb{R}^d$ acts as a physical point under those two forces until a physical equilibrium is obtained. The cross-entropy is now minimized between the two graphs. UMAP

returns an element of $\mathbb{R}^d$ for each element in the original dataset, using the cross-entropy of a graph on each of them.

Feature Measurements in the UMAP Embeddings. The UMAP approximation to this problem is based on comparing the differences among pre- and post-ablation studies by computing differences among their manifolds. In this way, the complete processing stage is created as follows. First, we defined the operator Φ^i_M, which is the UMAP transform optimized for ith pre-ablation case. Second, this operator is applied on ith pre- and post-ablation signals, creating two different manifolds which contain the latent information about the processed signals. This explanation can be summarized in a mathematical way by

$$M^i_{pre} = \Phi^i_M(X^i_{pre}),\ M^i_{post} = \Phi^i_M(X^i_{post}) \tag{22}$$

where M^{pre}_i (M^{post}_i) is the manifold computed for ith case, and X^i_{pre} (X^i_{post}) represents the input space, which can be compounded by P^l_j, their derivative, the time signal, among others.

Once the pre- and post-ablation manifolds are computed, the following step extracts features that can model the differences among pre- and post-ablation signals. For this purpose, we can define a manifold feature extractor, which is denoted as Φ_{MF}, and it represents the calculation of a new feature data vector

$$F^i_{pre} = \Phi^i_{MF}(M^i_{pre}),\ F^i_{post} = \Phi^i_{MF}(M^i_{post}) \tag{23}$$

where F^i_{pre} (F^i_{post}) is the manifold features vector computed for the ith case, and M^i_{pre} (M^i_{post}) represents the previously computed UMAP manifold for the ith case.

Preprocessing employed for the experiments in this section was slightly different from the one used in the previous section. For each recording, P-waves were segmented, and a Tukey window was applied to reduce the border effect. Afterward, signals were aligned by circular correlation, selecting those with a high correlation coefficient. Then, for each lead, five different P-wave templates were created by using 10, 25, 50, 75, and 90 percentiles from the previously highly correlated selected P-waves. Subsequently, ten time-shifted variants of each P-wave template were computed using the sliding window technique. After, the feature matrix was created by joining the P-wave templates, the time-shifted variants, and the time axis. Finally, once the feature matrices were computed for both registers from the same patient (pre- and post-ablation registers in the case of the AF ablation group individuals), they were normalized by z-score, taking the mean and standard deviation from the pre-ablation feature matrix.

On simulated BSPM records, feature extraction only varied in the preprocessing stage. Every single signal was cropped to get the P-wave depolarization, a Tukey window was applied to reduce the border effect, and they were aligned by circular correlation. After, the feature matrix was created by joining the preprocessed signals, and two different features were calculated, namely, $ValMax$, computed as the maximum of the absolute difference among pre- and post-ablation records on the same spatial position, and $PosMax$, computed as the time instant where the $ValMax$ value was reached.

5. Results

This section is structured as follows. First, a preprocessing and delineation stage was applied. In order to validate the algorithm developed in this previous stage, as well as to evaluate the quality of the ECG (absence of artifacts and noise), heuristic characteristics were obtained and compared in both control and AF ablation individuals. The previously computed features were used to feed a linear support vector machine (SVM) classifier designed to detect the AF ablation presence, in which the feature weights allowed us to scrutinize their relevance and interpretability. Second, the UMAP technique extracted crucial features from the previously used ECG database, and the classification performance was similarly benchmarked. Finally, the same approaches were used on simulated signals from the advanced atrial and torso models. This allowed us to quantify these detection techniques on not only standard leads but also whole torso registers and to obtain more detailed insight and clinical description of the role of the features obtained as relevant from patients.

5.1. Preprocessing, quality control, and heuristic features

P-wave stability among different beats was studied for control and AF ablation recordings. Fig. 4 depicts the template comprised of the median P-wave of the complete recording on a control (a) and AF ablation (b) subject, as well as the confidence intervals for the P-waves on both subjects (panels c and d). The control case presented high stability among the first (blue) and second (pink) follow-up recording P-waves, with similar confidence intervals. In contrast, the AF ablation case presented wider confidence intervals corresponding to the post-ablation recording (pink) compared to the pre-ablation recording (blue). Variations in duration and amplitude among pre- (blue) and post-ablation (pink) P-waves were stronger than for the control case. These differences observed between the control and AF ablation group appeared for any individual, which evidences that changes larger than the intrinsic variability of P-waves for a subject might be present in the P-wave morphology and duration after AF ablation.

We subsequently computed previously presented features (see Figs. 5,6,7). Features showed apparent differences among the control (blue) and AF ablation (orange) groups. On the one hand, P-waves templates showed a correlation coefficient (f_1) near 1 in control, whereas it turned lower in AF ablation, as shown in Fig. 5(a). On the other hand, the mean absolute difference (b) and normalized mean absolute difference (c) generally yielded greater scatter in AF ablation cases (f_2 and f_{2n}). Whole-beat template correlation (f_3) was used to check the method robustness Fig. 6(a). In this case, some variability can be seen due to noise and natural fluctuation, but in general, beat templates remained stable, thus indicating that the segmentation process was successful. Finally, features f_4, f_5, and f_6 were obtained from P-wave templates for both control and AF ablation groups. Differences in duration (Fig. 6(b)), amplitude (Fig. 6(c)), and area (Fig. 7(a)) were slighter for control patients compared to the ablation group, indicating that changes in morphology and duration can be seen after an AF ablation procedure. More substantial differences were observed in the case of amplitude and area features, while variations in duration were slight. All the calculations were supervised and adjusted in terms of preprocessing parameters to ensure data quality in the template comparisons and feature extraction. As depicted in Figs. 5,6,7 the increase of variability in the AF ablation group is better observed in different leads for different patients.

After applying a paired t-test for the control group, no significant differences were observed between P-waves templates of the first and second recordings in terms of duration and amplitude (as shown in Table 1, the null hypothesis was accepted with p-values of 0.1682 and 0.0821, respectively), whereas differences in the area were observed (p-value = 0.0012). In the case of the AF ablation group, significant differences among P-waves corresponding to pre- and post-ablation recordings were observed for all three features, which meant that changes in P-waves appeared after an ablation procedure. Finally, when comparing the control and AF ablation groups through an unpaired t-test before ablation (only the first recording for each individual was considered), no significant differences were visible for P-waves duration, amplitude, and area. For first and second control recordings and first and second AF ablation recordings, mean value ± standard deviation were, respectively: 0.0271 ± 0.0288, 0.0292 ± 0.0160, 0.0265 ± 0.0370 and 0.0299 ± 0.0376 s in case of P-wave duration; 0.0518 ± 0.0373, 0.0539 ± 0.0377, 0.0527 ± 0.0324 and 0.0458 ± 0.0322 mV in case of P-wave amplitude; 0.8336 ± 0.9063, 0.9453 ± 0.9362, 0.8546 ± 0.9413 and 0.5894 ± 0.9509 s·mV in case of P-wave area. Differences between pre- and post-ablation recordings are evident for the AF ablation group. In addition, bigger variability in P-wave duration, amplitude, and area can be observed for AF ablation individuals compared to controls.

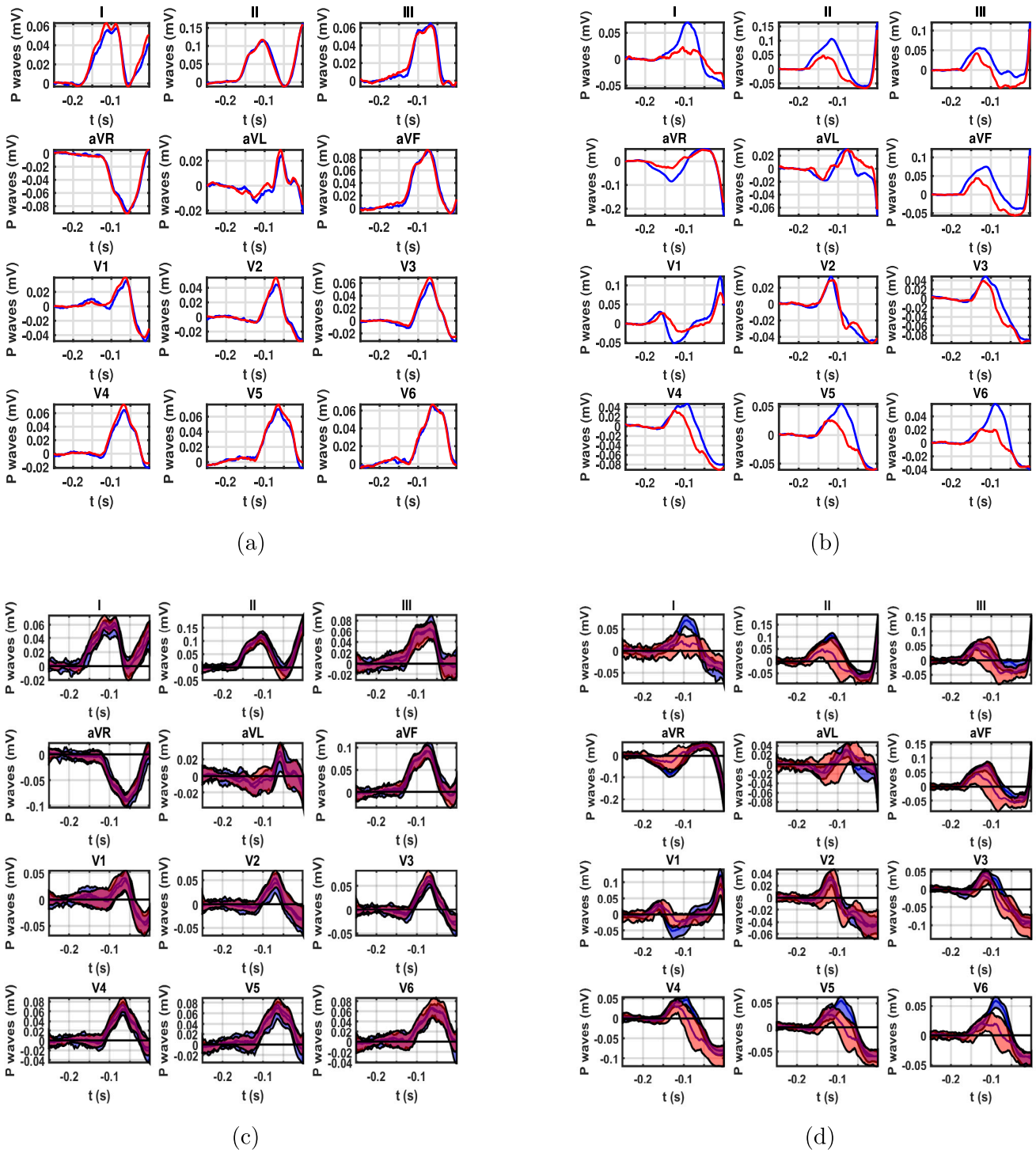

Fig. 4. P-wave templates and confidence intervals of the 12-lead ECG. Templates corresponding to a control (a) and an AF ablation (b) individual, obtained as the median P-wave of the whole 30-s recording, and confidence intervals of the P-waves corresponding to the same control (c) and AF ablation (d) individuals. Results associated with the first and second recordings are depicted in blue and pink, respectively.

Aiming to determine an indicator for a change detection system based on the tested features (f_1, f_2, f_{2n}, f_3, f_4, f_5, and f_6), a classifier was implemented using a linear SVM in order to get an interpretable classifier via its weights. The presented classifier exhibited a 77.78% accuracy. According to our previous results, duration and amplitude difference (f_4 and f_5) and correlation coefficient values (f_1) among pre- and post-ablation P-waves ruled the classification, as it can be seen in Fig. 7(b).

5.2. UMAP features and classification performance

To measure differences among pre- and post-ablation recordings, the UMAP algorithm was applied. Results are summarized in Figs. 8–10. Fig. 8, panels (a) and (b) show the Euclidean distance between the pre- and post-ablation embeddings for control and AF ablation groups, respectively. The control group generally exhibited lower distances than the AF ablation group. However, the border effect was

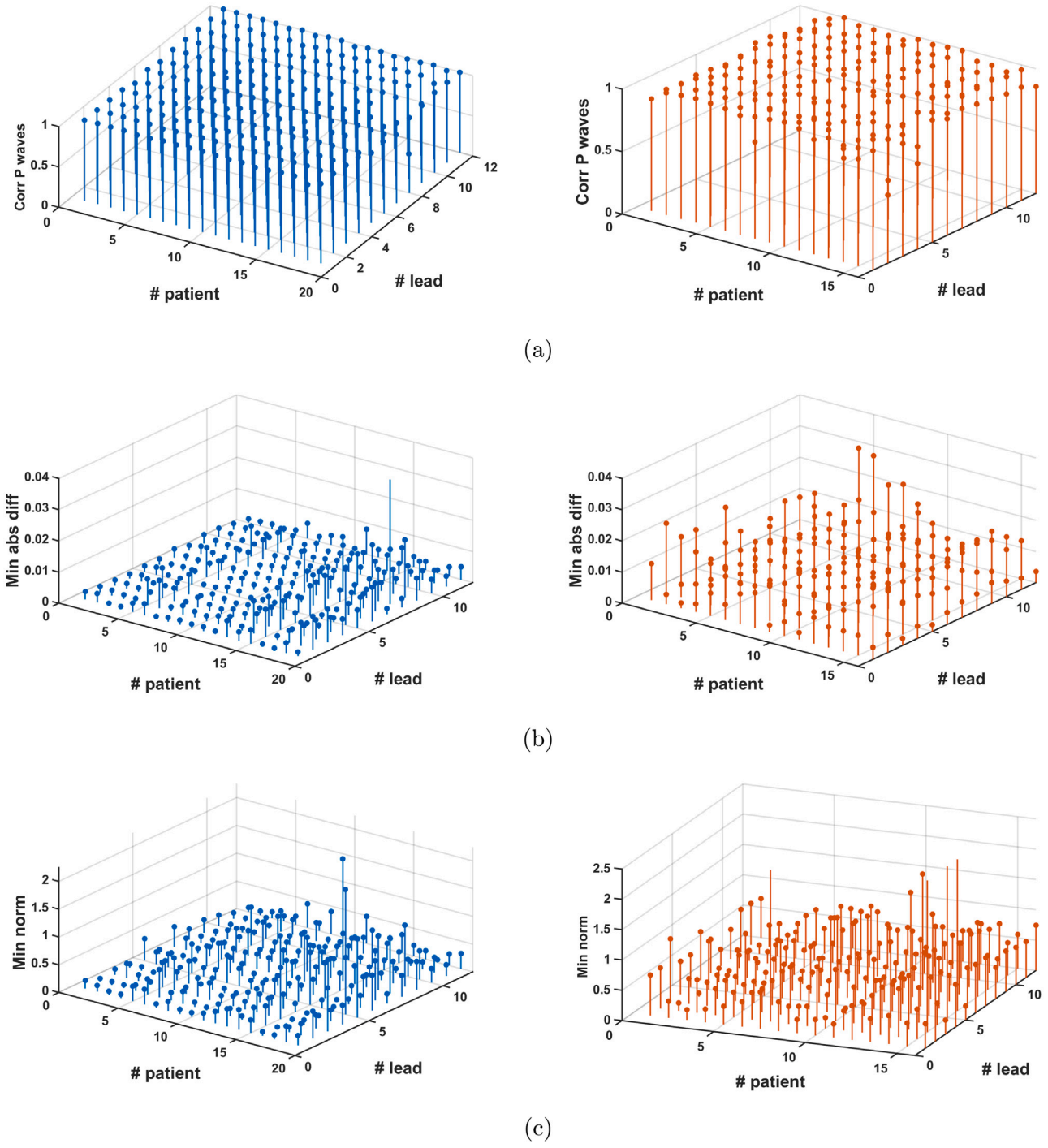

Fig. 5. Quality control and engineered features (f_1, f_2, f_{2n}) from P-wave (see text for further details). (a) Correlation metrics corresponding to the P-wave template (f_1); (b) mean absolute difference (f_2) and (c) normalized mean absolute difference (f_{2n}) between P-waves templates. Comparisons were made between both recordings about each patient. Graphs show features for all leads and all patients (the control group is shown in blue and the AF ablation group is in orange).

still noticeable in control due to the low performance of the UMAP for low amplitude inputs, as the first 50–75 samples corresponded to the baseline. This behavior can be better observed in panels (c) and (d), depicting an example of embedding for the control and AF ablation groups, respectively. In the control case (c), pre- (blue) and post-ablation (orange) embeddings were closer than in the AF ablation case (d). Nevertheless, this distance increased in the regions of the embeddings that correspond to the baseline in the recordings. Higher distances among pre- and post-ablation embeddings for the AF ablation group highlighted changes in P-waves after the AF ablation procedure. Fig. 9(a–d) shows the embedding distance metric over two control and AF registers. Orange colored background superimposed on the plots represents the segments of the recordings for which the pre- and post-ablation distance over-passed a threshold. It should be noted the proper functioning of the method. Distance values were low in those control cases, with negligible differences between both recordings. They did not reach the threshold (b). In contrast, in AF ablation cases with differences between the pre- and post-ablation recordings, distance values were high, over-passed the threshold, and segments of the recordings with remarkable morphological differences were indicated with the orange-colored background (d). Therefore, this method was able to discriminate between pre- and post-ablation recordings. However, it

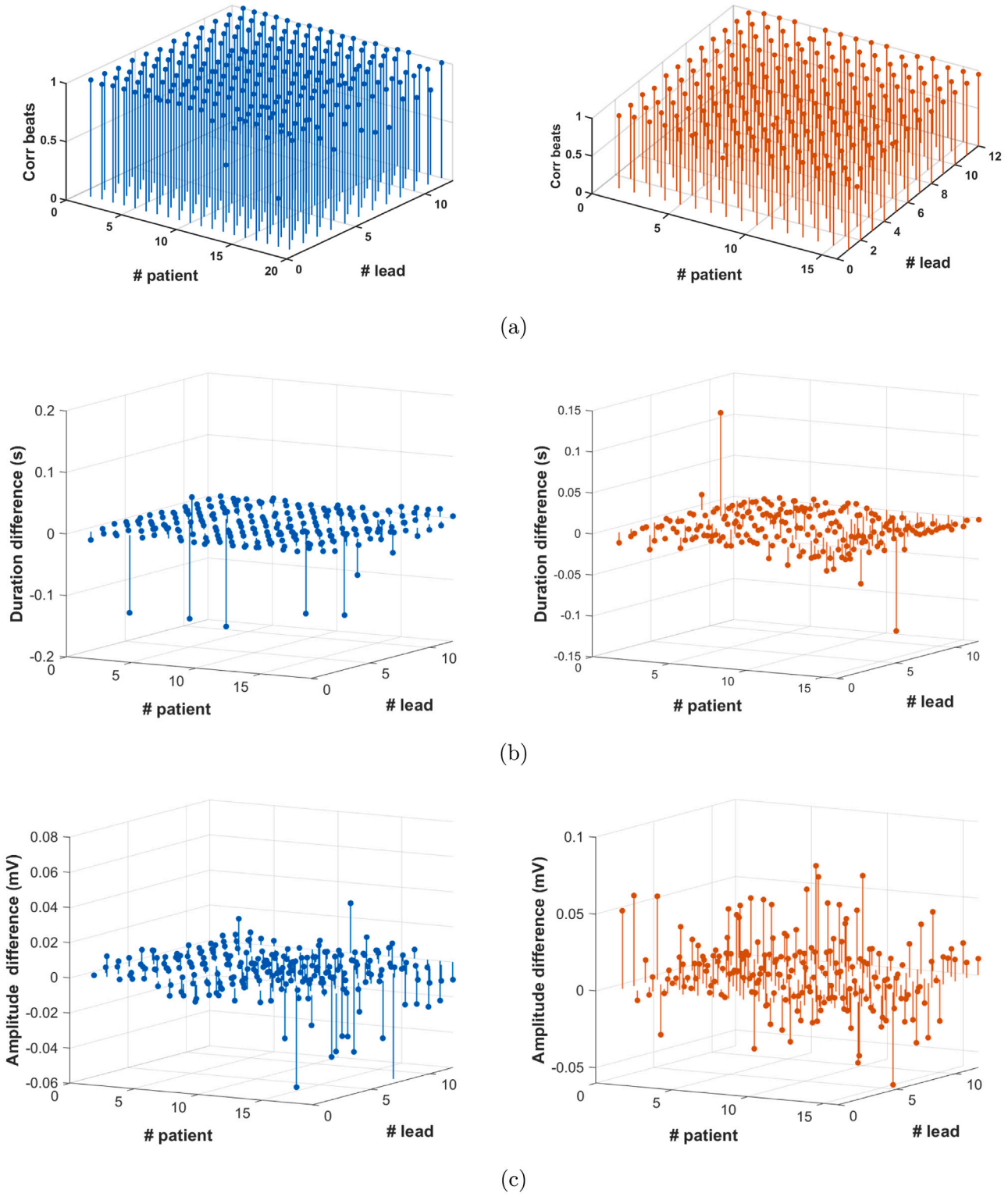

Fig. 6. Quality control and engineered features (f_3, f_4, f_5) from P-wave (see text for further details). (a) Correlation metrics corresponding to the whole beat template (f_3); (b) differences in duration (f_4) and (c) differences in amplitude (f_5) for P-wave templates. Comparisons were made between both recordings about each patient. Graphs show features for all leads and all patients (the control group is shown in blue and AF ablation group is in orange).

might fail in this discrimination for those control cases showing strong P-wave morphology changes (a) or those AF ablation cases with slight changes on P-waves before and after the ablation procedure (c).

Finally, after processing each patient, a linear SVM was used to classify the registers as control or AF ablation groups according to the previously computed pre- and post-ablation embedding distance, resulting in a classifier with 94.44% accuracy. Fig. 10 shows the classifier weights. As depicted, higher weights in the classification correspond to the region over 125 to 200 samples. This is the P-wave position in the considered window (concretely, the last part of the P-wave).

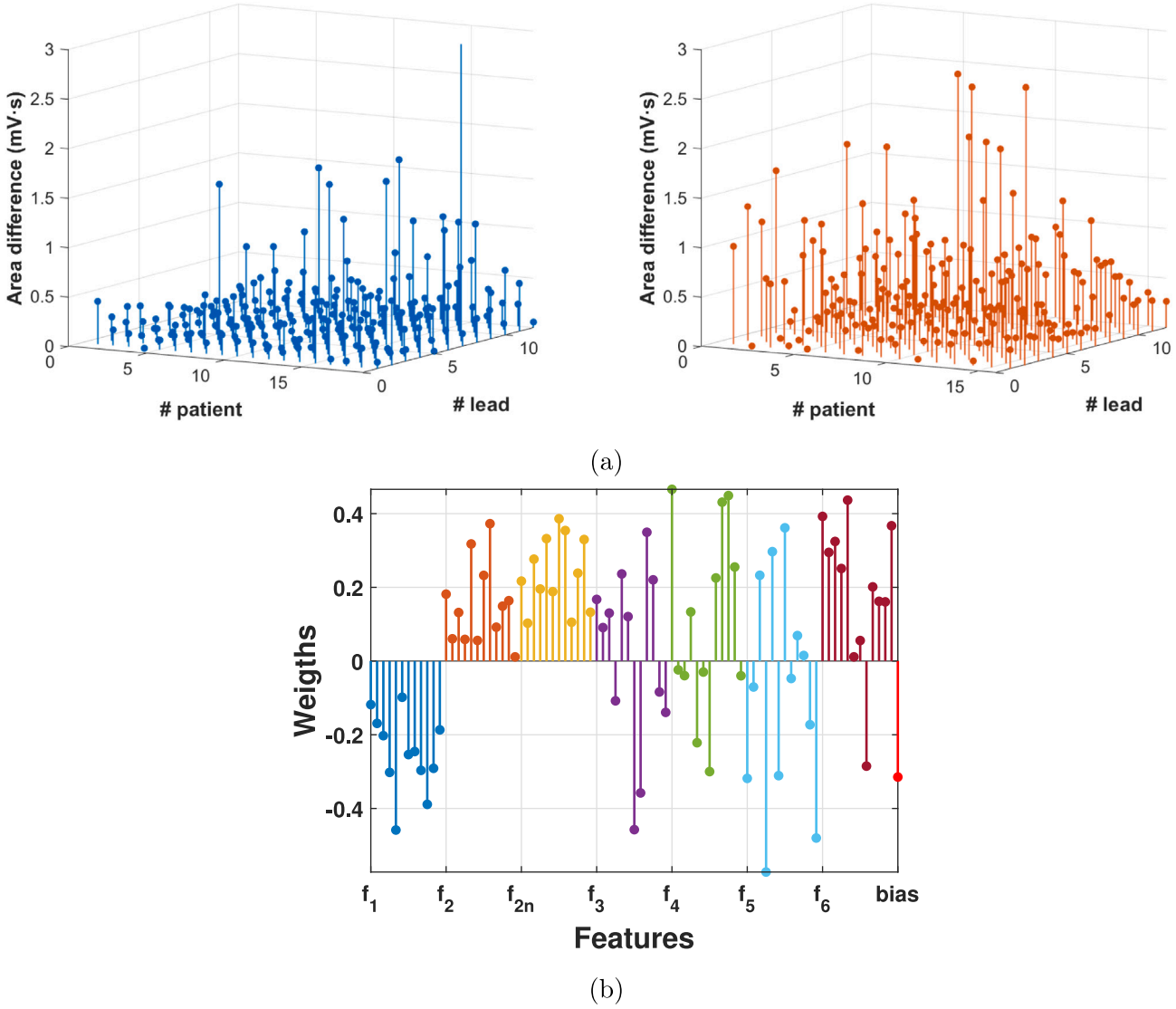

Fig. 7. Quality control and engineered features (f_6) from P-wave (see text for further details). (a) Differences in areas (f_6) for P-wave templates. Comparisons were made between both recordings about each patient. Graphs show features for all leads and all patients (the control group is shown in blue and AF ablation group is in orange). (b) Linear SVM weights for f_1, f_2, f_{2n}, f_3, f_4, f_5, f_6, and bias. Different colors are used for each feature.

Although an exhaustive comparison between different automatic feature extraction methods is out of the scope of this work, the t-SNE and PCA (Principal Components Analysis) [28] methods were also tested. In the case of the t-SNE method, there was no clear differentiation between control and AF ablation groups regarding the detection of P-wave changes after ablation. In addition, this method does not allow the projection of the second recordings on the first recording embedded space to see the time differences between them (in the case of the AF ablation group, these recordings correspond to the pre- and post-ablation signals). On the contrary, the PCA method, which also reduces the dimensionality but allows the mentioned projection, showed larger P-wave differences for the AF ablation group than for the control group. However, when these results were used to feed a linear SVM classifier designed to detect P-wave changes and thus, the AF ablation presence, the classifier exhibited a 72.22% accuracy, compared to the 77.78% and 94.44% obtained with conventional features extraction and the UMAP method, respectively.

5.3. Results on advanced simulations

In this section, computational simulations were used to check whether differences observed in P-wave morphology from patients can also be detected in a virtual patient. We also scrutinized whether standard leads are recording those differences or whether it would be recommendable to use additional leads to detect PV isolation and future potential AF ablation reconnections.

For this purpose, simulated P-wave recordings over the whole torso surface (P^T) were used. The processing applied to simulated signals was slightly different from that used with clinical data (see Section 4.1 for further details). Then, features extraction was performed using heuristic methods (f_4, f_5, and f_6, obtained according to previously computed fiducial points) and the UMAP algorithm. Simulation results summarized in Figs. 11 and 12 agree with clinical results obtained from patients since standard leads showed differences among pre- and post-ablation recordings. Color-coded spatial information provided by torso maps (Fig. 11) showed that P-wave differences over the torso surface were observed for both UMAP and heuristic maps, with slight variations among maps regarding the region of the torso where they are visible. Maps built with UMAP information depicted, on the one hand, the position of the maximum difference between the pre- and post-ablation recordings for all nodes within the torso surface, and on the other hand, the value of this difference. Both map patterns resembled, although the maximum value map showed the most decisive differences between

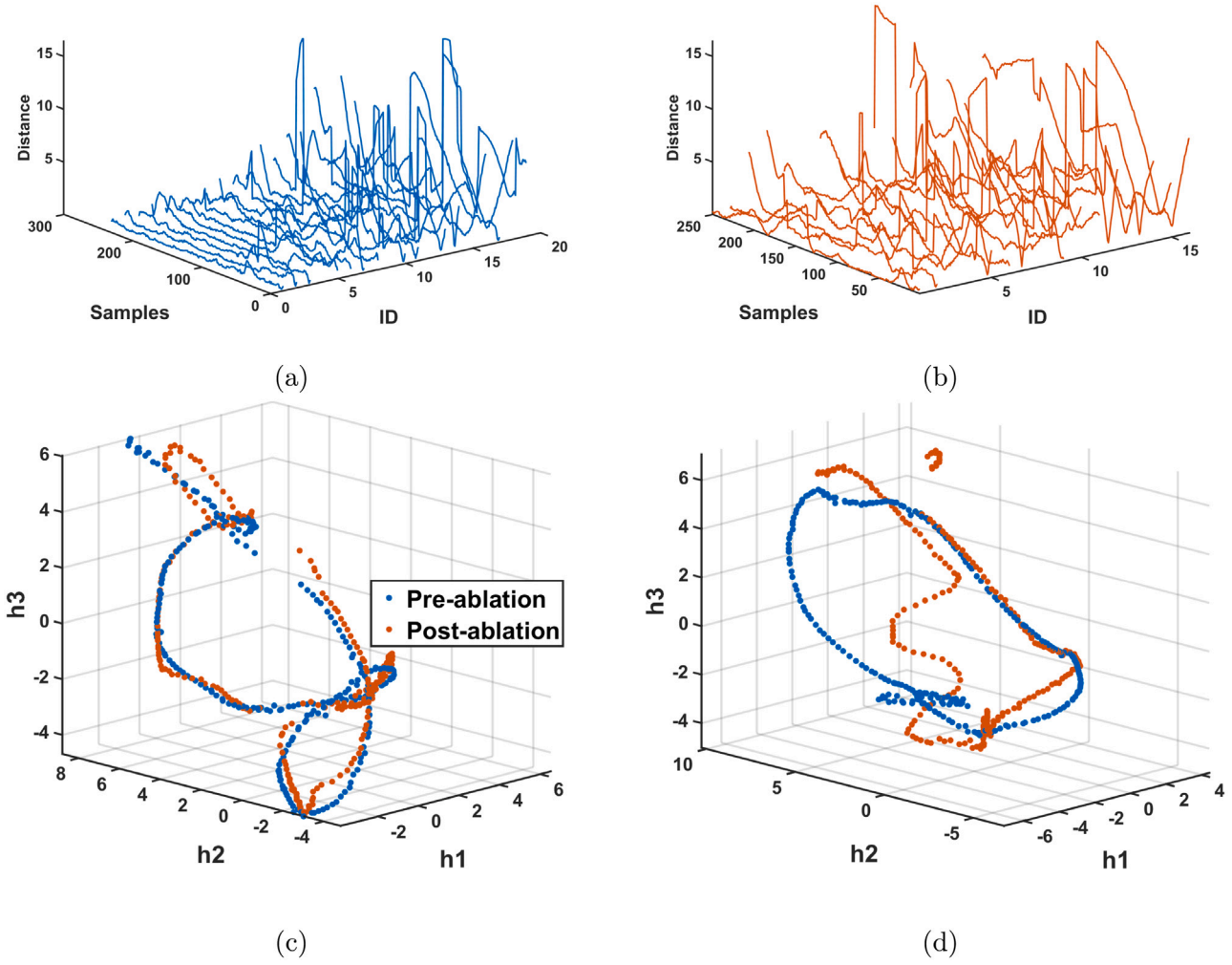

Fig. 8. Different measurements and examples from UMAP latent features. The Euclidean distance among pre- and post-ablation embedding spaces for control (a) and AF ablation (b) groups. Embedding example for control (c) and AF ablation (d) registers (pre-ablation projection in blue, post-ablation projection in orange). In the control group, no ablation was performed, and pre- and post-ablation recordings correspond to two different recordings from the same patient unrelated to an ablation procedure.

pre- and post-ablation limited to smaller regions on the torso, compared to the position map.

Regarding maps based on heuristic features, they had similar patterns in which maximum differences can be observed in the same region on the torso surface. Duration, amplitude, and area maps correspond to the absolute value of the difference between the P-wave duration (f4), amplitude (f5), and area (f6) of pre- and post-ablation recordings. The duration map is much more inhomogeneous than the amplitude map, probably due to the high sensitivity of the Phasor Transform method [23] to slight variations in the recordings when detecting the P-wave offset compared to the detection of the P-wave peak. Map discontinuities appeared in torso regions close to the atria, where local activation containing different wavefronts propagating in different directions produced strong fluctuations in the simulated P-waves. More homogeneous regions were those far from the atria, containing smoother P-waves. Transitions on the amplitude map for neighboring electrodes were smoother than in the case of the duration map. As a result, the amplitude map was much more regular, with a broad region of maximum differences in the center of the top anterior torso and below the diagonal between the left shoulder and the mid-right side of the posterior torso. Finally, the area map mixed patterns described by the duration and amplitude maps.

In general, as observed in Fig. 11, the color-coded torso maps suggested several regions on the torso surface different from the standard leads location to be the best position to record maximum differences in P-waves after an ablation procedure. Therefore, we located three different grids of 9 electrodes in different regions on the torso surface to cover the maximum differences shown by all the maps. The first and second grids of electrodes, called *front 1* and *front 2*, respectively, were located in the anterior torso, whereas the third grid, called *back*, was set in the posterior torso. They are shown in Fig. 11 over the maps (pink, white and green). In addition, electrodes corresponding to the standard leads are also depicted over the maps in gray. Fig. 12(a–d) shows the P-waves corresponding to each of the nine electrodes for the front 1, front 2, and back grids and the standard leads, respectively. For each panel, differences between pre- (blue) and post-ablation (orange) P-waves can be observed. However, those differences seemed visually more significant for the front 2 (b) and back (c) grids compared to the front 1 grid (a), and standard leads electrodes (d). Panel (e) shows the signal resulting from the subtraction of the post-ablation to the pre-ablation P-wave. As expected, differences in the first half of the P-wave (before the red dotted line) were minimal, while in the second half (after the red dotted line), they considerably increased. This was

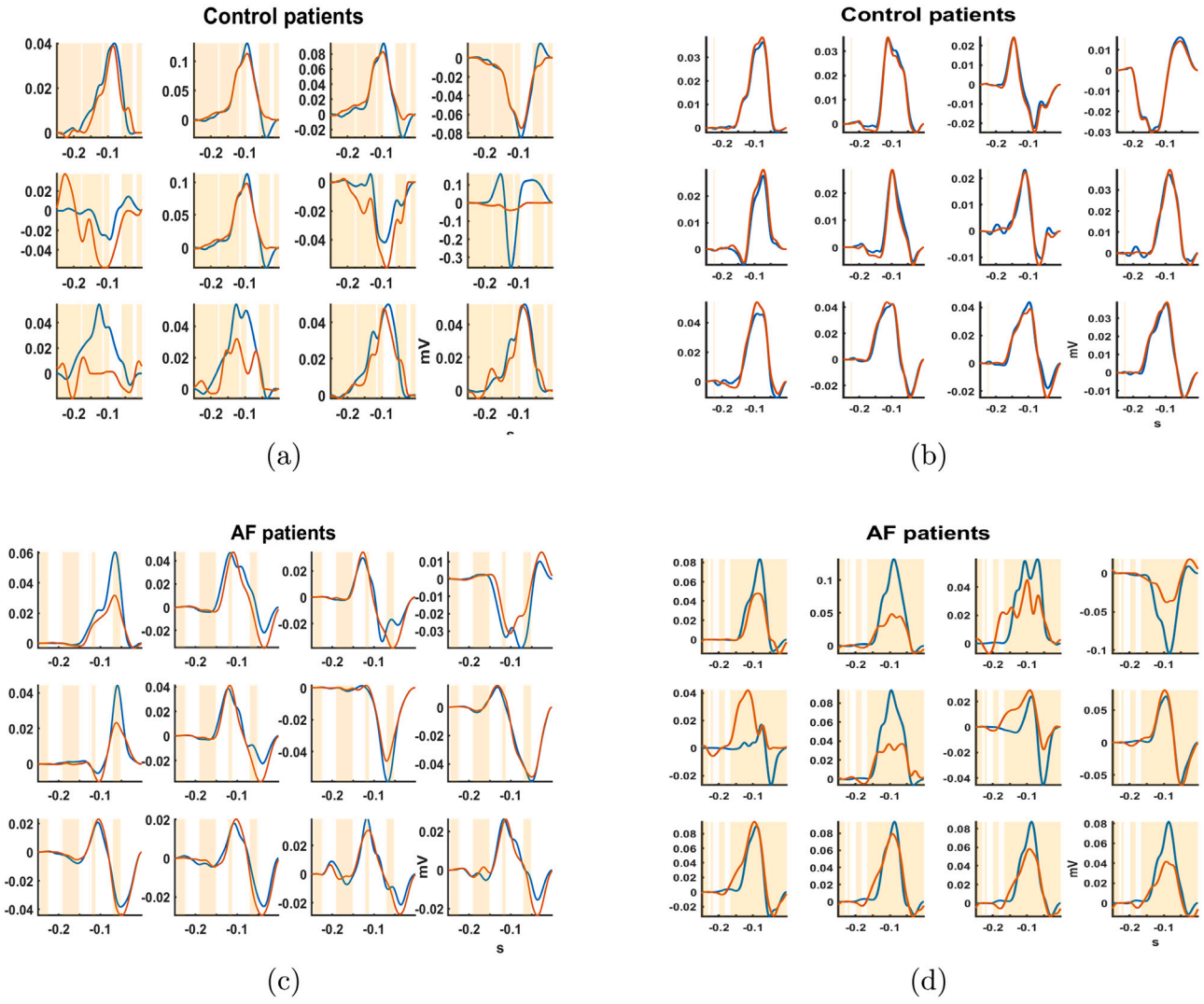

Fig. 9. Examples of control registers with a high (a) and low (b) embedding distance metric value, and AF ablation registers with a low (c) and high (d) embedding distance metric value (pre-ablation recording in blue, post-ablation in orange). Low (high) values of the embedding distance metric indicate the absence (existence) of pre- and post-ablation differences. In the control group, no ablation was performed, and pre- and post-ablation recordings correspond to two different recordings from the same patient unrelated to an ablation procedure.

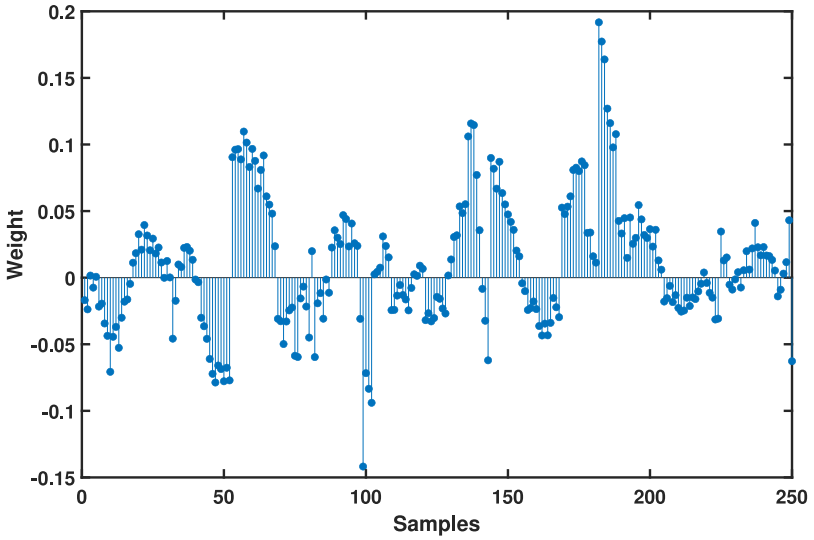

Fig. 10. Classification weights for a linear SVM classifier made for an input space of UMAP latent features.

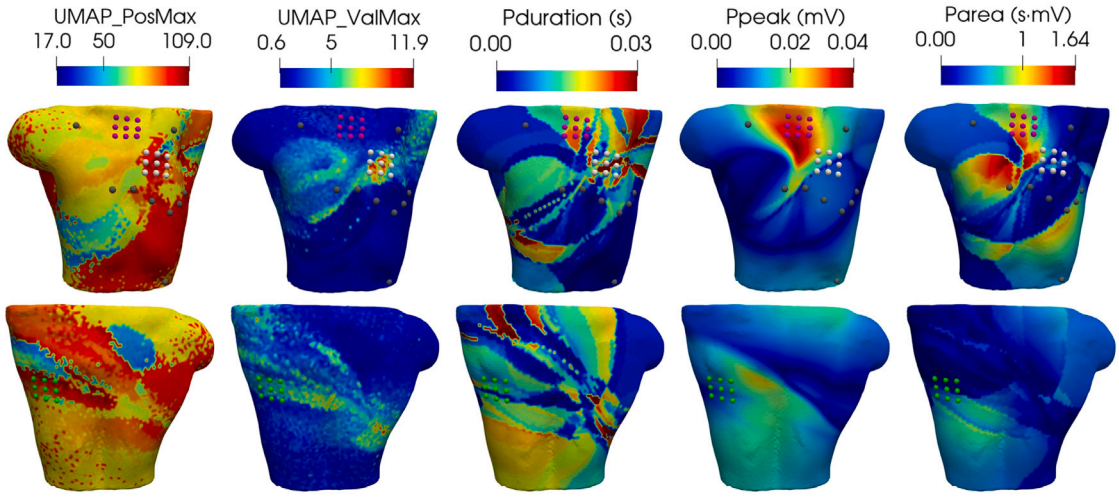

Fig. 11. Color-coded maps on the virtual patient. From left to right: UMAP features (position and value of the maximum difference) and heuristic features (f_4, f_5 and f_6). Top row: anterior torso; bottom row: posterior torso. Electrodes corresponding to the standard leads are depicted in gray, grid 1 in pink (front 1), grid 2 in white (front 2), and grid 3 in green (back).

Table 1
Comparison between P-waves of both recordings for the control (top) and AF ablation (middle) group, and between the first recording of both groups (bottom). h0 is the null hypothesis; CI is confidence interval.

	Control group		
	h0	p-value	CI
Duration	0	0.1682	[−0.0051, 0.0008]
Amplitude	0	0.0821	[−0.0046, 0.0002]
Area	1	0.0012	[−0.1785, −0.0448]
	AF-Abl. group		
	h0	p-value	CI
Duration	1	0.0052	[−0.0058, −0.0010]
Amplitude	1	3.44×10^{-5}	[0.0037, 0.0101]
Area	1	1.22×10^{-7}	[0.1701, 0.3603]
	Control vs AF-Abl. group		
	h0	p-value	CI
Duration	0	0.8552	[−0.0057, 0.0069]
Amplitude	0	0.7958	[−0.1986, 0.1566]
Area	0	0.8165	[−0.0077, 0.0059]

due to the PV isolation since PVs contribute to the last part of the P-wave. Finally, to quantify whether standard leads were optimal when detecting changes in P-waves after ablation or, on the contrary, the suggested grids of electrodes better-collected P-waves variations, we calculated the root mean square (RMS) of the signals shown in panel (e). Panel (f) depicts a boxplot for each grid tested, and the standard leads electrodes for the first half of the P-wave (top), the second half of the P-wave (middle), and the whole P-wave duration (bottom). The RMS value of the difference signal in each electrode is depicted. The differences between different grids and standard leads were minimal in the first half of the P-wave. However, in the second half of the P-wave, the front 1 and front 2 grids clearly showed more significant differences than the standard leads and the back grid. In addition, the front 2 grid and the standard leads showed higher variability between electrodes, probably due to the irregular maps in the regions where those electrodes were located. Nevertheless, as shown in panels (a)–(d), P-waves amplitudes vary among grids and between different electrodes in the same grid, and absolute values of the observed differences might falsify results. Therefore, the bottom graph in panel (f) shows the RMS values of the normalized signals in (e). In this case, the grid that better detects P-waves variations among pre- and post-ablation signals is front 2, followed by the standard leads, front 1, and finally, the back grid. As before, the front 2 grid and the standard leads presented higher variation between different electrodes concerning the changes observed in the P-waves. The front 1 and back grids presented more stable results among their electrodes.

6. Discussion

Clinical evidence suggests that, after the process of ablation of the PVs as a therapeutic tool for the elimination of AF, on many occasions, fibrillation processes recur. In this direction, and with the aim of validating the existence of real and complete electrophysiological isolation of the PVs, in this work we have carried out a thorough analysis of the P-wave before and after ablation. To do so, we evaluated the success of the presented procedure, by comparing conventional extraction of characteristics on clinical and simulated ECG signals with automatic extraction based on integrated signal processing using the UMAP method. The novelty of this study is that: (1) the UMAP algorithm can overcome one of the limitations of the ablation procedures since it can be used as a non-invasive technique to verify proper PVs isolation during the intervention without prolonging it, and without the need of the ECG delineation; (2) the UMAP algorithm can also be used during follow-up visits as a non-invasive technique to check that the PVs are still disconnected; (3) additional leads seem to be necessary on the anterior and posterior torso to better detect proper PVs disconnection.

On the P-wave Variability and UMAP Features. The variability of the P-wave is an accepted fact for cardiac electrophysiology. However, according to the literature, severe alterations of its parameters have been described concerning cardiac affections, especially in AF conditions. Variations in the P-wave morphology leading to a primary and a secondary P-wave template [29], prolonged duration of the P-wave [30,31] and a significant variability over the intrinsic dispersion of the P-wave interval [32] have been pointed out as AF indicators. In this work, we found less P-wave variability over time for control individuals than for AF ablation patients, which is in agreement with literature [33]. In addition, we hypothesized that after an ablation procedure, P-wave changes might occur. These differences could be used as an indicator of the PVs isolation success and to detect later reconnections in follow-up recordings for those patients who underwent an AF ablation procedure. Our results confirmed this hypothesis. Statistically significant differences were observed between the pre- and post-ablation recordings for heuristic features (duration, amplitude, and area). They were corroborated with UMAP results, in which euclidean distances between the pre- and post-ablation embeddings were smaller for the

Fig. 12. Differences between pre- and post-ablation simulated recordings. P-waves corresponding to front 1 (a), front 2 (b), and back (c) grids, and standard leads (d). Pre- and post-ablation recordings in blue and orange, respectively. Difference between the pre- and post-ablation recording for each electrode (e), with signals from front 1 grid in blue, front 2 in yellow, back in green and standard leads in purple. The red dotted line splits the P-wave into two halves. Root mean square values (f) from signals in (e) for the first half (top) and the second half (middle) of the P-waves and for the whole P-wave duration when normalizing signals by their maximum (bottom).

control than for the AF ablation group. Although the UMAP algorithm has already been applied to ECG signals for dimensionality reduction and features extraction [34], to our knowledge, this is the first work using it to detect P-waves changes after PVs isolation. The accuracy of the classifier to discriminate between control and AF ablation groups improved when feeding the SVM with UMAP characteristics instead of with conventional heuristic features (94.44% versus 77.78%).

On the Simulation Results. In terms of the P-wave analysis, results obtained for in-silico modeling are consistent with our results derived from clinical data and the findings in the literature. In particular, the synthetic models studied here and the tools developed made it possible to visualize variations in the duration and morphology of the P-wave, mainly in its last part, as a result of the sharp reduction of the electrophysiological activity due to the ablated tissue. The use of standard 12-lead ECG for AF remains limited to its diagnosis in clinical practice [35]. In this work, we proposed new use for the ECG. On the one hand, it can be used to check if PV isolation was successful during an ablation procedure. On the other hand, it can later detect potential PVs reconnection during follow-up visits and prior AF recurrences. Furthermore, in in-silico simulations, we observed that variations in P-waves after PVs isolation were not homogeneous over the whole torso surface. This led us to suggest the location of additional electrodes to the standard leads in those regions on the anterior and posterior torso surface with more substantial differences. BSPM has already been used for the study of AF organization, and complexity [36–38]. However, to our knowledge, this is the first work that employs BSPM to detect PV isolation using P-wave analysis.

In addition, it has been demonstrated that when translating this methodology to clinical practice, there is no need to record potentials over the whole torso surface. Only a few electrodes well located on the anterior torso, over the region of the precordial leads, and on the posterior torso, near the left scapula, are necessary. A previous simulation work [24] stated that left PVs contribution to the P-wave was better observed in this region of the posterior torso. Petrutiu and colleagues also demonstrated that RA and LA frequency gradients can be non-invasively monitored by using additional posterior lead recordings since LA electrical activity is better observed in posterior torso locations [39]. This is in agreement with our results. Torso maps showed considerable differences between pre- and post-ablation recordings near the left scapula, where we suggested setting a grid of electrodes. However, although differences on the posterior torso seemed to be better concentrated in the last part of the P-wave, recordings are of lower amplitude in this region. Therefore, differences are lower than in the anterior torso recordings. In our simulations, the most substantial differences appeared on the anterior torso, over the precordial leads, where we also suggested locating additional electrodes. This might be because we are simulating cryo-ablation. Therefore, a comprehensive portion of the LA besides the PVs was ablated. Consequently, this ablated region's lack of contribution to the P-waves might be seen in the anterior torso. Finally, it should be noted that maps built based on UMAP characteristics and heuristic features present a similar trend regarding the pre- and post-ablation differences patterns. However, UMAP information yielded less noisy and more homogeneous maps.

On the Ablation Implications. Clinical consensus establishes the ablation method as the most effective procedure to isolate PVs. On the other hand, the verification of the success of this procedure supposes prolonging the intervention or carrying out another equally invasive subsequent procedure. The existence of a non-invasive procedure that allows both verifications at the time of the intervention, and later in time for periodic monitoring of any possible re-connections, is considered of great interest since it would allow its review in non-hospital outpatient systems [40,41].

Limitations and future work. This work focused on detecting P-wave changes after PV isolation. For this purpose, we compared conventional feature extraction (P-wave fiducial points detection and P-wave duration, amplitude, and area calculation) with the automatic UMAP algorithm. The major limitation of this study might be related to the size of the patient database. In future works we expect to increase the number of recruited individuals and to extend the study to patients with reconnections and to the analysis of intermediate signals, after each PV isolation, to detect potential reconnections and locate the PV to be isolated again in order to avoid AF recurrences.

Another limitation of this study is that we did not exhaustively compare the UMAP algorithm with other methods for feature extraction to find the best method for this clinical application, as it was out of the scope of this work. UMAP results were only compared to PCA and t-SNE methods, the UMAP method yielding better performance. Since the main goal of this study was to detect P-waves changes after PV isolation without ECG delineation and fiducial points detection due to the limitations associated with this type of method, and the best results were obtained with the UMAP algorithm, we chose it as a proof-of-concept to solve this clinical problem. Additional research to find the best method for this clinical application could be carried out as a future independent study by testing, among others, autoencoders.

7. Conclusion

In this work, we demonstrated that AF ablation drives singular and recognizable P-wave changes. Those changes can be used to check PVs isolation success during the procedure and it might be useful to evaluate persistent PVs isolation in patients with arrhythmia recurrences. We also demonstrated that the UMAP method can be a promising alternative to the heuristic characterization of P-waves (i.e., those employing features such as duration, amplitude, or area). The former is less prone to noise and avoids potential inaccuracies due to the delineation process of the fiducial points. Furthermore, it allows for highly accurate classification of ECG recordings between two different groups: control and AF ablation. In addition, computational models and simulations showed their value in enhancing the information retrieval from clinical data. They suggest that standard leads are not optimal for detecting PVs isolation, and additional leads on the anterior and posterior torso should be used for better achievements in P-wave ablation.

Declaration of competing interest

The authors declare the following financial interests/personal relationships which may be considered as potential competing interests: A. García-Alberola declares institutional research and tuition fees from Medtronic Ibérica.

Acknowledgments

This work was partially supported by research Grant PID2019-104356RB-C41, PID2019-104356RB-C42, PID2019-104356RB-C43, and PID2019-106623RB-C41 funded by MCIN/AEI/10.13039/501100011033, and by research Grant PROMETEO/2020/043 funded by Generalitat Valenciana. It was also partially supported by Grant SC-LEARNING-CM funded by Next Generation REACT-UE and Grant 2023/00004/032-F924 and 2023/00004/030-F923 funded by Universidad Rey Juan Carlos.

References

[1] G. Hindricks, N. Dagres, E. Arbelo, J. Bax, C. Blomström-Lundqvist, G. Boriani, 2020 ESC guidelines for the diagnosis and management of atrial fibrillation developed in collaboration with the European association for cardio-thoracic surgery (EACTS): The task force for the diagnosis and management of atrial fibrillation of the European society of cardiology (ESC) developed with the special contribution of the European heart rhythm association (EHRA) of the ESC, Eur. Heart J. 42 (5) (2021) 373–498.

[2] K. Barret, H. Brooks, S. Boitano, S. Barman, Ganong's Review of Medical Physiology, twenty third ed., McGraw Hill, 2010.

[3] J.A. Cabrera, G. Pizarro, D. Sánchez-Quintana, Transmural ablation of all the pulmonary veins: Is it the Holy Grail for cure of atrial fibrillation? Eur. Heart J. 31 (22) (2010) 2708–2711, http://dx.doi.org/10.1093/eurheartj/ehq241, arXiv:https://academic.oup.com/eurheartj/article-pdf/31/22/2708/1325553/ehq241.pdf.

[4] J.G. Andrade, Cryoballoon ablation for pulmonary vein isolation, J. Cardiovasc. Electrophysiol. 31 (8) (2020) 2128–2135.

[5] Y. Nakatani, T. Sakamoto, K. Mizumaki, K. Nishida, N. Kataoka, Y. Tsujino, Y. Yamaguchi, H. Inoue, Coefficient of variation of P-wave duration is a novel atrial heterogeneity index to predict recurrence of atrial fibrillation after catheter ablation, J. Cardiovasc. Electrophysiol. 27 (5) (2016) 542–548.

[6] Y. Nakatani, T. Sakamoto, Y. Yamaguchi, Y. Tsujino, N. Kataoka, K. Kinugawa, Coefficient of variation of P-wave duration measured using an automated measurement system predicts recurrence of atrial fibrillation, J. Electrocardiol. 53 (2019) 79–84.

[7] E.J. da S. Luz, W.R. Schwartz, G. Cámara-Chávez, D. Menotti, ECG-based heartbeat classification for arrhythmia detection: A survey, Comput. Methods Programs Biomed. 127 (2016) 144–164, http://dx.doi.org/10.1016/j.cmpb.2015.12.008.

[8] F.-M. Melgarejo-Meseguer, E. Everss-Villalba, F.-J. Gimeno-Blanes, M. Blanco-Velasco, Z. Molins-Bordallo, J.-A. Flores-Yepes, J.-L. Rojo-Álvarez, A. García-Alberola, On the beat detection performance in long-term ECG monitoring scenarios, Sensors 18 (5) (2018) 1387.

[9] P. Harikrishna, S.J. Hussain, A comprehensive review on accurate QRS and T wave detection techniques for confirming cardiac abnormalities, in: 2019 International Conference on Recent Advances in Energy-Efficient Computing and Communication, ICRAECC, IEEE, 2019, pp. 1–6.

[10] L. McInnes, J. Healy, J. Melville, Umap: Uniform manifold approximation and projection for dimension reduction, 2018, arXiv preprint arXiv:1802.03426.

[11] M. Li, Y. Si, W. Yang, Y. Yu, ET-UMAP integration feature for ECG biometrics using stacking, Biomed. Signal Process. Control 71 (2022) 103159.

[12] B. Taccardi, B. Punske, R. Lux, R. MacLeod, P. Ershler, T. Dustman, Y. Vyhmeister, Useful lessons from body surface mapping, J. Cardiovasc. Electrophysiol. 9 (7) (1998) 773–786.

[13] A. Pullan, M. Buist, L. Cheng, Mathematically Modelling the Electrical Activity of the Heart: From Cell to Body Surface and Back Again, World Scientic, 2005.

[14] J. Heijman, P. Abdoust, N. Voigt, S. Nattel, D. Dobrev, Computational models of atrial cellular electrophysiology and calcium handling, and their role in atrial fibrillation, J. Physiol. 594 (3) (2016) 537–553.

[15] L. Martinez-Mateu, L. Romero, A. Ferrer-Albero, R. Sebastian, J.F. Rodríguez Matas, J. Jalife, O. Berenfeld, J. Saiz, Factors affecting basket catheter detection of real and phantom rotors in the atria: A computational study, PLoS Comput. Biol. 14 (3) (2018) 1–26, http://dx.doi.org/10.1371/journal.pcbi.1006017.

[16] M. Courtemanche, R.J. Ramirez, S. Nattel, Ionic mechanisms underlying human atrial action potential properties: Insights from a mathematical model, Am. J. Physiol.-Heart Circ. Physiol. 275 (1) (1998) H301–H321, http://dx.doi.org/10.1152/ajpheart.1998.275.1.H301, PMID: 9688927.

[17] L. Martinez-Mateu, L. Romero, J. Saiz, O. Berenfeld, Far-field contributions in multi-electrodes atrial recordings blur distinction between anatomical and functional reentries and may cause imaginary phase singularities — A computational study, Computers in Biology and Medicine 108 (2019) 276–287, http://dx.doi.org/10.1016/j.compbiomed.2019.02.022, https://www.sciencedirect.com/science/article/pii/S0010482519300691.

[18] E.A. Heidenreich, J.M. Ferrero, M. Doblaré, J.F. Rodríguez, Adaptive macro finite elements for the numerical solution of monodomain equations in cardiac electrophysiology, Ann. Biomed. Eng. 38 (2010) 2331–2345, http://dx.doi.org/10.1007/s10439-010-9997-2.

[19] D.B. Geselowitz, W.T. Miller 3rd, A bidomain model for anisotropic cardiac muscle, Ann. Biomed. Eng. 11 (3–4) (1983) 191–206.

[20] A. Vadillo-Valderrama, R. Goya-Esteban, R.P. Caulier-Cisterna, A. García-Alberola, J.L. Rojo-Álvarez, Differential beat accuracy for ECG family classification using machine learning, IEEE Access 10 (2022) 129362–129381, http://dx.doi.org/10.1109/ACCESS.2022.3227219.

[21] E. Everss-Villalba, F.M. Melgarejo-Meseguer, M. Blanco-Velasco, F.J. Gimeno-Blanes, S. Sala-Pla, J. Rojo-Álvarez, A. García-Alberola, Noise maps for quantitative and clinical severity towards long-term ECG monitoring, Sensors 17 (2017) 2448.

[22] P. Bloomfield, Fourier Analysis of Time Series, second ed., in: Wiley Series in Probability and Statistics, John Wiley & Sons, Nashville, TN, 2000.

[23] A. Martínez, R. Alcaraz, J.J. Rieta, Application of the phasor transform for automatic delineation of single-lead ECG fiducial points, Physiol. Meas. 31 (11) (2010) 1467–1485.

[24] A. Ferrer, R. Sebastián, D. Sánchez-Quintana, J. Rodríguez, E. Godoy, L. Martínez, J. Saiz, Detailed anatomical and electrophysiological models of human atria and torso for the simulation of atrial activation, PLoS One 10 (11) (2015) e0141573.

[25] L. van der Maaten, G. Hinton, Visualizing data using t-SNE, J. Mach. Learn. Res. 9 (2008) 2579–2605.

[26] C. Péalat, G. Bouleux, V. Cheutet, Improved time series clustering based on new geometric frameworks, Pattern Recognit. 124 (2022) 108423.

[27] M. Belkin, P. Niyogi, Laplacian eigenmaps for dimensionality reduction and data representation, Neural Comput. 15 (2003) 1373–1396.

[28] J.E. Jackson, A User's Guide to Principal Components, John Wiley & Sons, 2005.

[29] D. Filos, I. Chouvarda, D. Tachmatzidis, V. Vassilikos, N. Maglaveras, Beat-to-beat P-wave morphology as a predictor of paroxysmal atrial fibrillation, Comput. Methods Programs Biomed. 151 (2017) 111–121, http://dx.doi.org/10.1016/j.cmpb.2017.08.016.

[30] G.O. Furniss, D. Panagopoulos, S. Kanoun, E.J. Davies, D.R. Tomlinson, G.A. Haywood, The effect of atrial fibrillation ablation techniques on p wave duration and p wave dispersion, Heart, Lung Circ. 28 (3) (2019) 389–396.

[31] R. Pranata, E. Yonas, R. Vania, Prolonged P-wave duration in sinus rhythm pre-ablation is associated with atrial fibrillation recurrence after pulmonary vein isolation—A systematic review and meta-analysis, Ann. Noninvasive Electrocardiol. 24 (5) (2019) e12653.

[32] S. Shrestha, O. Chen, M. Greene, J.J. John, Y. Greenberg, F. Yang, Change in p wave morphology after convergent atrial fibrillation ablation, Indian Pacing Electrophysiol. J. 16 (1) (2016) 3–7.

[33] F. Censi, I. Corazza, E. Reggiani, G. Calcagnini, E. Mattei, M. Triventi, G. Boriani, P-wave variability and atrial fibrillation, Sci. Rep. 6 (2016) 26799.

[34] M. Li, Y. Si, W. Yang, Y. Yu, ET-UMAP integration feature for ECG biometrics using stacking, Biomed. Signal Process. Control 71 (2022) 103159.

[35] T.A.R. Lankveld, S. Zeemering, H.J.G.M. Crijns, U. Schotten, The ECG as a tool to determine atrial fibrillation complexity, Heart 100 (14) (2014) 1077–1084, http://dx.doi.org/10.1136/heartjnl-2013-305149.

[36] P. Bonizzi, M. Guillem, A. Climent, J. Millet, V. Zarzoso, F. Castells, O. Meste, Noninvasive assessment of the complexity and stationarity of the atrial wavefront patterns during atrial fibrillation, IEEE Trans. Biomed. Eng. 57 (9) (2010) 2147–2157, http://dx.doi.org/10.1109/TBME.2010.2052619.

[37] L.Y. Di Marco, J.P. Bourke, P. Langley, Spatial complexity and spectral distribution variability of atrial activity in surface ECG recordings of atrial fibrillation, Med. Biol. Eng. Comput. 50 (2012) 439–446, http://dx.doi.org/10.1007/s11517-012-0878-8.

[38] M. Meo, T. Pambrun, N. Derval, C. Dumas-Pomier, S. Puyo, J. Duchâteau, P. Jaïs, M. Hocini, M. Haïssaguerre, R. Dubois, Noninvasive assessment of atrial fibrillation complexity in relation to ablation characteristics and outcome, Front. Physiol. 9 (2018) 929, http://dx.doi.org/10.3389/fphys.2018.00929.

[39] S. Petrutiu, A.V. Sahakian, W. Fisher, S. Swiryn, Manifestation of left atrial events and interatrial frequency gradients in the surface electrocardiogram during atrial fibrillation: Contributions from posterior leads, J. Cardiovasc. Electrophysiol. 20 (2009) 1231–1236, http://dx.doi.org/10.1111/j.1540-8167.2009.01523.x.

[40] P. Liu, T. Lv, Y. Yang, Q. Gao, P. Zhang, Use of p wave indices to evaluate efficacy of catheter ablation and atrial fibrillation recurrence: A systematic review and meta-analysis, J. Intervent. Cardiac Electrophysiol. (2022) 1–14.

[41] Y. Miao, M. Xu, L. Yang, C. Zhang, H. Liu, X. Shao, Investigating the association between P wave duration and atrial fibrillation recurrence after radiofrequency ablation in early persistent atrial fibrillation patients, Int. J. Cardiol. 351 (2022) 48–54.